Chapter 2
Preparation of Nanosize Silicon-Nitride-Based Ceramics and Their Superplasticity

2.1 Introduction

Silicon-nitride-based ceramics have been widely studied, largely in response to the desire to manufacture internal combustion engines entirely from ceramics. Programs attempting to realize a ceramic engine have achieved only partial success, but the associated research has led to a comprehensive understanding of Si_3N_4 ceramics. Si_3N_4-based components now have a wide range of industrial applications owing to their unique combination of excellent mechanical properties and good corrosion and thermal shock resistance [1]. However, their good mechanical properties greatly increase the cost of manufacturing complex components from them. The application of superplastic deformation is attracting considerable interest as a novel method for the net-shape fabrication of Si_3N_4 components.

The superplasticity of Si_3N_4-based ceramics was first reported by Wakai et al. for a Si_3N_4/SiC nanocomposite in the early 1990s [2]. Tensile elongation of up to 150 % was achieved at a strain rate of 4×10^{-4} s^{-1} at 1600 °C. Since then, numerous silicon nitride ceramics have been demonstrated to exhibit superplastic behavior under different stress and temperature conditions [3–6].

In the development of superplastic ceramics, high ductility and a high deformation rate are the primary objectives. Practical considerations further require that these properties should be achieved at the lowest temperature possible. The requirement of a high deformation rate and a low deformation temperature lies in the constitutive equation of superplastic flow, which can be expressed in the following form:

$$\dot{\varepsilon} = A \cdot \frac{\sigma^n}{d^p} \cdot \exp\left(\frac{-Q}{RT}\right), \tag{2.1}$$

T. Nishimura and X. Xu, *Fabrication of Heat-Resistant and Plastic-Formable Silicon Nitride*, NIMS Monographs, DOI 10.1007/978-4-431-55384-7_2

where $\dot{\varepsilon}$ is the strain rate, σ is the flow stress, A is a temperature-dependent, diffusion-related coefficient, n and p are the stress and grain-size exponents respectively, d is the grain size, Q is the activation energy, and RT is the gas constant multiplied by the absolute temperature. For superplastic ceramics, n and p are typically between 1 and 3. Therefore, a high deformation rate and a low deformation temperature can be achieved by the following steps:

(i) Increasing the grain boundary diffusivity, which can be achieved by introducing a transient liquid phase or a more viscous liquid phase [5, 6]. Chen and coworkers used the transient-phase approach to prepare sialon materials, that exhibited excellent superplasticity due to enhanced grain boundary sliding in the large transient liquid phase [5, 6].
(ii) Reducing the grain size. Nano-sized Si_3N_4 ceramics are expected to exhibit good superplasticity, which is very important for the cost-effective near-net-shape forming of complex ceramic components. Kim et al. reported high-strain-rate superplasticity in a nano-sized composite of zirconia, alumina, and spinel with a large tensile elongation of 1050 % at a strain rate of 0.4 s^{-1} [7].

Nanomaterials have been a fast-growing field of research in the past 30 years. In the beginning, metals were mainly investigated. Later, a large amount of research was conducted on nanoceramic materials [8]. In addition to excellent superplasticity [2, 7], increased hardness, bending strength, Weibull modulus, and abrasive wear resistance have also been observed in these nanoceramics [9].

Many studies have also been carried out to fabricate Si_3N_4-based ceramics with even finer grains. However, dense Si_3N_4-based nanoceramics are very difficult to prepare. The first Si_3N_4 ceramic with nanosize grains was reported in 1995 by Nishimura et al. [10]. Fine homogeneous β-Si_3N_4 powder with an average particle size of 280 nm was used as the starting powder. To prevent the abnormal grain growth of β-Si_3N_4, spark plasma sintering (SPS) has been applied. In the SPS process, raw powders in a carbon die are pressed uniaxially and a direct current (d.c.) pulse voltage is applied. At an early stage of the procedure, the powders are heated by spark discharge between the particles. The carbon die is also heated by a d.c. pulse voltage so that the powder is heated from both inside and outside. Therefore, SPS provides very rapid heating (higher than 300 °C/min) in a very short time (within minutes) to enable the full densification of powder materials [11]. By applying SPS, grain growth can be suppressed to a large degree. A homogeneous microstructure with an average grain size of about 200–300 nm was obtained by Nishimura et al. [10] after sintering at 1600 °C for 7 min, as shown in Fig. 2.1.

Comparing the particle size of the starting powder and the Si_3N_4 grains in the sintered body, it is concluded that SPS can prevent rapid grain coarsening during the sintering process. Thus, to achieve nano-sized Si_3N_4 ceramics with a grain diameter of less than 100 nm, a nano-sized silicon nitride starting powder is necessary.

However, nano-size Si_3N_4 powders generally exist in an amorphous form. Li et al. have studied the densification of nano-sized amorphous Si_3N_4 powders

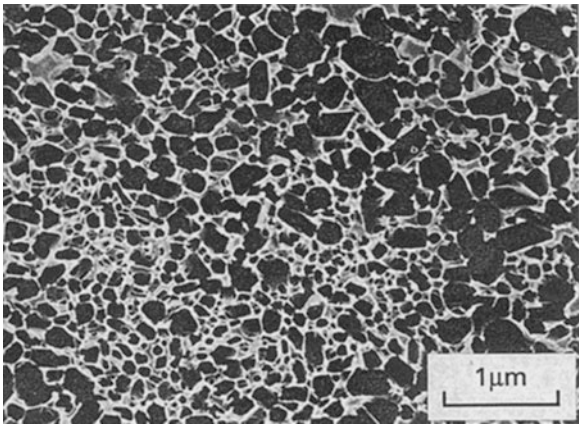

Fig. 2.1 Microstructure of Si_3N_4 nanoceramic fabricated by SPS at 1600 °C for 7 min with sintering additives of 5 wt% Y_2O_3 + 2 wt% MgO [10]

without additives under ultrahigh pressure (1.0–5.0 GPa) [12]. These nanopowders could be pressed to a high density (87 %), even at room temperature, under ultrahigh pressure; however, rapid grain growth occurred during the crystallization, leading to a grain size (>160 nm) almost one order of magnitude greater than the starting particulate diameter (about 18 nm), indicating that it is impossible to obtain nano-sized Si_3N_4 ceramics using amorphous Si_3N_4 starting powders.

High-energy mechanical milling can be used to synthesize a variety of equilibrium and nonequilibrium alloy phases [13], in which the processing of a solid-state powder involves repeated welding, fracturing, and rewelding of the powder particles. Compared with conventional milling, high-energy mechanical milling is superior in terms of producing bulk quantities of nanocrystalline materials using simple equipment at room temperature [14]. Thus, it is expected to be used to decrease the particle size of starting Si_3N_4 powders.

2.2 Preparation of Dense Nano-Sized Si_3N_4 Ceramics

2.2.1 Si_3N_4 Ceramics

A submicrometer β-Si_3N_4 powder (NP500 grade, Denki Kagaku Kogyo Co., Tokyo, Japan) with an average particle size of 0.2 μm was selected as the starting powder. The sintering additives were 5 mol% Y_2O_3 (99.9 % pure, Shin-etsu Chemical Co., Tokyo, Japan) and 2 mol% Al_2O_3 (99.9 % pure, Sumitomo Chemical Co., Tokyo, Japan). All powders were mixed in ethanol using Si_3N_4 balls for 4 h. The as-received powder mixture, denoted as P0, was then mechanically milled at a high energy using silicon nitride balls of 5 mm diameter and a silicon nitride pot of 350 ml volume. The ball-to-powder weight ratio was 20:1, the milling speed was 475 rpm, and the milling time was 4 h. The powder mixture obtained is denoted as P2.

The XRD patterns of the P0 and P2 powders are shown in Fig. 2.2. After high-energy mechanical milling, the peaks of the starting powders and the sintering additives were significantly weakened (Si_3N_4) or disappeared completely (Y_2O_3 and Al_2O_3), and a highly diffuse background structure could be seen, indicating that most of the P2 powder was transformed into an amorphous state. The residual β-Si_3N_4 peaks were greatly broadened, suggesting significant refinement of the particle size of crystalline β-Si_3N_4. The corresponding TEM image, selected-area diffraction pattern (SADP), and HRTEM image of the P2 powder (Fig. 2.3) confirm the amorphization of the starting powder and the sintering additives and the existence of nano-sized Si_3N_4 particles with a diameter of about 10 nm.

Unlike the powder obtained from laser chemical vapor precipitation [12], the nanocrystalline powder features many agglomerated particles with a diameter of 100–200 nm. Each agglomerate consists of many nanocrystalline β-Si_3N_4 particles. This unique property of the high-energy mechanically milled powder helps suppress rapid grain growth during sintering, as shown later.

As mentioned before, to prevent the nanosize particles in the powder from growing rapidly into large grains during ordinary sintering owing to the very high driving force, the nanopowder precursor was subjected to SPS. The shrinkage curves of the P0 and P2 powders sintered at 1600 °C for 5 min are plotted in Fig. 2.4. The onset of liquid phase formation and densification for P0 occurs at about 1350 °C (corresponding to the formation of the ternary eutectic phase at 1345 °C in the SiO_2–Al_2O_3–Y_2O_3 system). Although the onset shrinkage temperature is slightly higher for P2, the shrinkage increases abruptly at about 1550 °C. The observed maximal shrinkage rates ($-d(\Delta L/L_0)/dt$) were calculated to be 0.08 and 0.004 s^{-1} for P2 and P0, respectively, indicating the very rapid densification of P2.

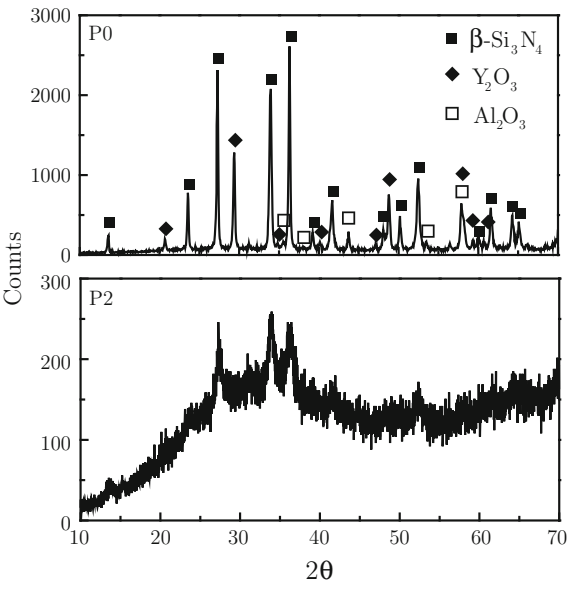

Fig. 2.2 XRD patterns of P0 and P2 powders

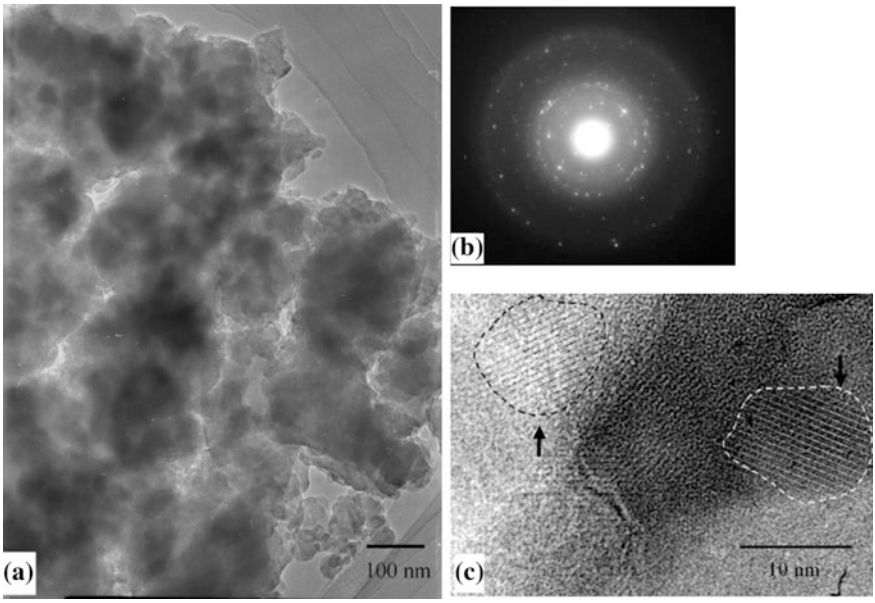

Fig. 2.3 Morphology of P2 powder: **a** TEM image, **b** SADP, **c** HRTEM image, in which nanocrystalline β-Si_3N_4 particles are indicated by *dashed lines*

Figure 2.5 shows the effect of the sintering temperature on the bulk density of P0 and P2 for the same holding time of 5 min. The P2 powder is completely densified at a sintering temperature of 1600 °C, which is about 150 °C lower than that for the as-received P0 powder.

The microstructure for P2 after sintering (1600 °C, 5 min) is shown in Fig. 2.6. Note the very fine grains with a size of about 68 nm and the narrow grain size distribution. The XRD pattern shows that the sintered Si_3N_4 nanoceramic consists of 100 % β-Si_3N_4.

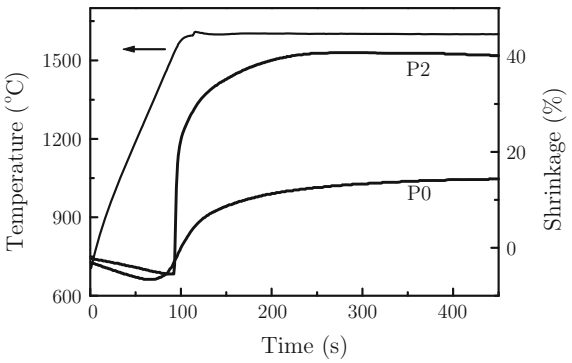

Fig. 2.4 Shrinkage curves of P0 and P2 powders

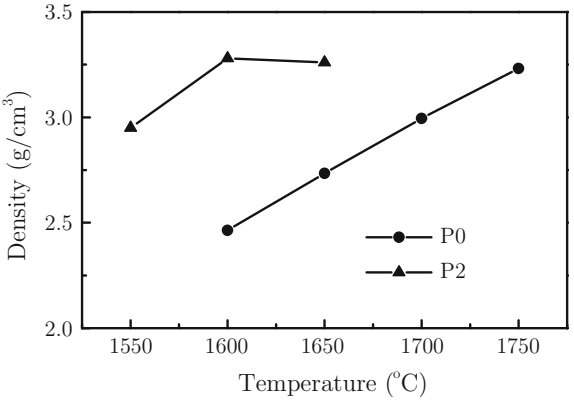

Fig. 2.5 Effect of sintering temperature on density of sintered P0 and P2 powders for the same holding time of 5 min

The densification of Si_3N_4 ceramics is described on the basis of the liquid-phase sintering mechanism formulated by Kingery [15]: (i) particle rearrangement due to liquid-phase formation, in which the extent of densification mainly depends on the particle size and shape and the amount of the liquid phase and its viscosity; (ii) solution-diffusion-precipitation which initiates the solution of materials at contact points between particles and a center-to-center approach accompanied by grain growth; and (iii) a coalescence stage, in which minor densification through grain coarsening occurs.

As mentioned above, the liquid phase plays an important role in both the densification and grain growth of Si_3N_4 ceramics. Here, as a result of high-energy mechanical milling, the sintering additives in P2 react with Si_3N_4 to form a large quantity of a nitrogen-rich amorphous Y–Al–Si–O–N phase containing supersaturated Si_3N_4 [16]. Upon heating, the amorphous phase in P2 softens and melts, whereas eutectic liquid-phase Y–Al–Si–O starts to form in P0. Because the viscosity of oxynitride glass increases significantly with increasing nitrogen content [16], the onset shrinkage temperature of P2 is slightly higher than that of P0 (Fig. 2.4). Compared with P0, however, P2 contains a larger amount of the liquid phase and much finer β-Si_3N_4 particles, meaning that P2 can be densified more rapidly than P0 during its rearrangement, i.e., the first stage of densification, with the assistance of applied pressure. In addition, rapid heating makes it possible to densify nearly all the powder precursor before precipitation ends or the solution-diffusion-precipitation process starts.

The liquid phase in P2 is a nonequilibrium alloy phase of supersaturated Si_3N_4 [16]. At high temperatures, β-Si_3N_4 crystals precipitate from the liquid phase with a very high driving force, and the uniform dispersion of Si_3N_4 nanoparticles in the liquid phase favors homogeneous precipitation. Following precipitation, grain growth starts. The achievement of nano-sized grains in dense Si_3N_4 ceramics is attributed to the following factors. First, grain coarsening is suppressed by crystal impingement due to the homogeneously dispersed Si_3N_4 crystals and the high density achieved before grain growth occurs. Second, the β-phase is used as the

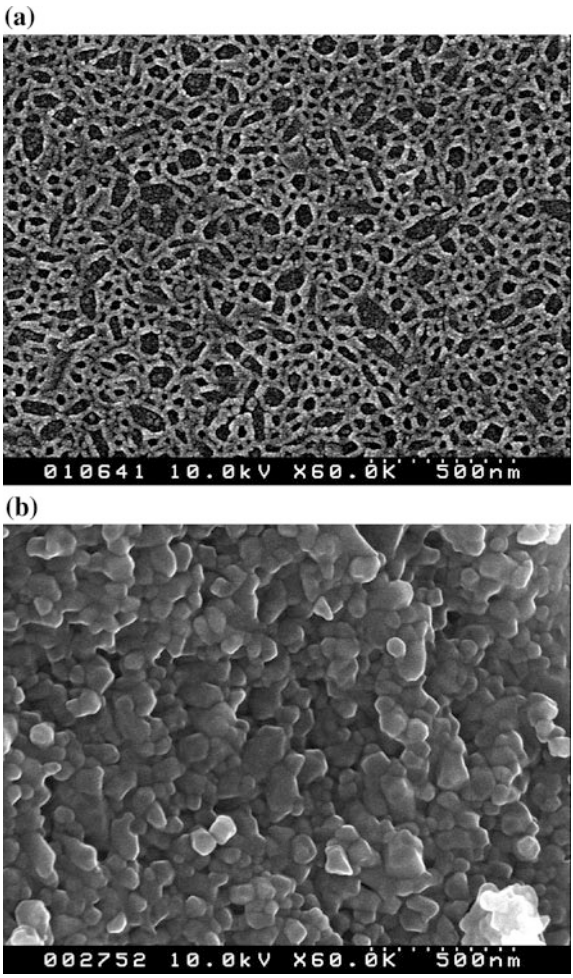

Fig. 2.6 Microstructure of P2 powder after sintering at 1600 °C for 5 min: **a** etched polished surface, **b** fracture surface

starting powder, thus avoiding the $\alpha \rightarrow \beta$ phase transformation and leading to a low driving force for grain growth, third, the high sinterability of high-energy mechanically milled powders decreases the sintering temperature significantly and shortens the holding time. Finally, the high viscosity of the nitrogen-rich liquid phase suppresses grain coarsening in P2. On the basis of the above observations, the final grain size in dense Si_3N_4 nanoceramics is expected to depend on the number and size of nanocrystalline β-Si_3N_4 particles dispersed in the milled powders. Finer Si_3N_4 nanoceramics are anticipated if the number of nanocrystalline β-Si_3N_4 particles is increased and their size is decreased by optimizing the milling parameters.

In conclusion, dense nano-sized Si_3N_4 ceramics were successfully prepared via high-energy mechanical milling and subsequent SPS. In the following sections, the proposed method will be applied to prepare nano-sized Si_3N_4-based ceramics.

2.2.2 Sialon Ceramics

Sialon ceramics have better high-temperature properties and higher hardness than Si_3N_4 ceramics because of the smaller amount of the intergranular glassy phase [17]. β-Sialons, which were the first of the sialon family to be developed, are formed by substituting up to two-thirds of the Si in β-Si_3N_4 with Al while ensuring valency compensation by replacing an equivalent concentration of N with O to obtain a range of β-sialons, $Si_{6-z}Al_zO_zN_{8-z,}$ with $0 < z < 4.2$. Since the difference between the bond lengths of Si–N and Al–O is small (0.174 nm for Si–N and 0.175 nm for Al–O), the lattice strain is also small and the amount of replacement has a wide range [17].

A starting mixture with the nominal composition Si_5AlON_7 ($z = 1$) was mixed in ethanol using silicon nitride balls for 4 h. The as-received powder mixture (denoted as BP0), with a mass of about 6.2 g, was then subjected to high-energy mechanical milling with the same milling parameters as mentioned above. The amorphization of the starting powders during mechanical milling also occurred and milled powders (denoted as BP2) with a similar structure were obtained.

The as-received powders (BP0) and milled powders (BP2) were subjected to SPS at different temperatures with the same holding time of 5 min. As can be seen in Fig. 2.7, the BP2 powder is nearly completely densified at 1550 °C, while the BP0 powder almost reaches its theoretical density at 1650 °C. The densification temperature for BP2 is about 100 °C lower than that for the as-received BP0 powder.

Figure 2.8 shows the β-sialon content and the calculated z-value for samples of BP0 and BP2 after sintering at different temperatures, as calculated from the XRD patterns. Only β-Si_3N_4 and β-sialon peaks were detected in the XRD patterns for all samples. The β-sialon content of all the samples of BP2 is 100 %, while it is low in samples of BP0, indicating that high-energy mechanical milling promotes the phase transformation by the amorphization of the starting powders. The calculated z-values of β-sialon for samples taken from BP2 are always 1 as designed

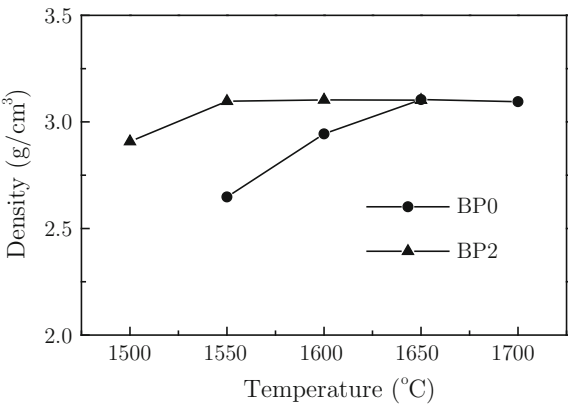

Fig. 2.7 Effect of sintering temperature on density of sintered BP0 and BP2 powders for the same holding time of 5 min

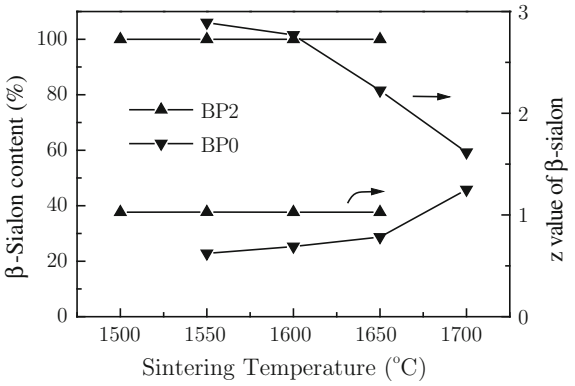

Fig. 2.8 β-sialon content and z-value of β-sialon after sintering at different temperatures

(the oxidation of starting powders during milling was avoided), whereas those for samples taken from BP0 are much higher than 1, indicating that the β-sialon grains that initially formed are richer in Al and O than the overall composition, which is in good agreement with results reported in the literature [18], although α-Si_3N_4 powder was used as the starting powder in [18]. As can also be seen from Fig. 2.8, the β-sialon content and the calculated z-value for the samples taken from BP0 approach equilibrium with increasing temperature.

Figures 2.9 and 2.10 show the fracture surfaces of dense ceramics sintered at different temperatures obtained from the BP2 and BP0 powders, respectively. Densification at lower temperatures and the existence of nanocrystalline Si_3N_4 after milling, as for the BP2 specimens, can also influence the grain size of the final dense ceramics. The BP0 powder produces coarse equiaxed grains with an average size of about 1 μm, while the BP2 powder leads to homogeneously dispersed fine equiaxed grains with an average size of about 50 nm (1550 °C) and 60 nm (1600 °C). It is concluded that the proposed method is effective for fabricating β-sialon nanoceramics.

Many researchers have studied the densification and phase transformation of β-sialon ceramics from the starting powders of Si_3N_4, AlN, and Al_2O_3 [18, 19]. Transient liquid-phase sintering (similar to the liquid-phase sintering mechanism formulated by Kingery) is generally used to describe the process, which is considered to proceed in three (partly overlapping) stages:

Stage 1: Particle rearrangement immediately following the formation of the liquid phase.
Stage 2: A solution-diffusion-reprecipitation process, which involves the solution of materials at the contact points between particles and a center-to-center approach. This stage also involves the solution of small grains and reprecipitation on large grains, so it is accompanied by grain growth. As the densification proceeds, most of the liquid phase is incorporated into the newly formed sialon grains.
Stage 3: A coalescence stage, in which minor densification through grain coarsening occurs.

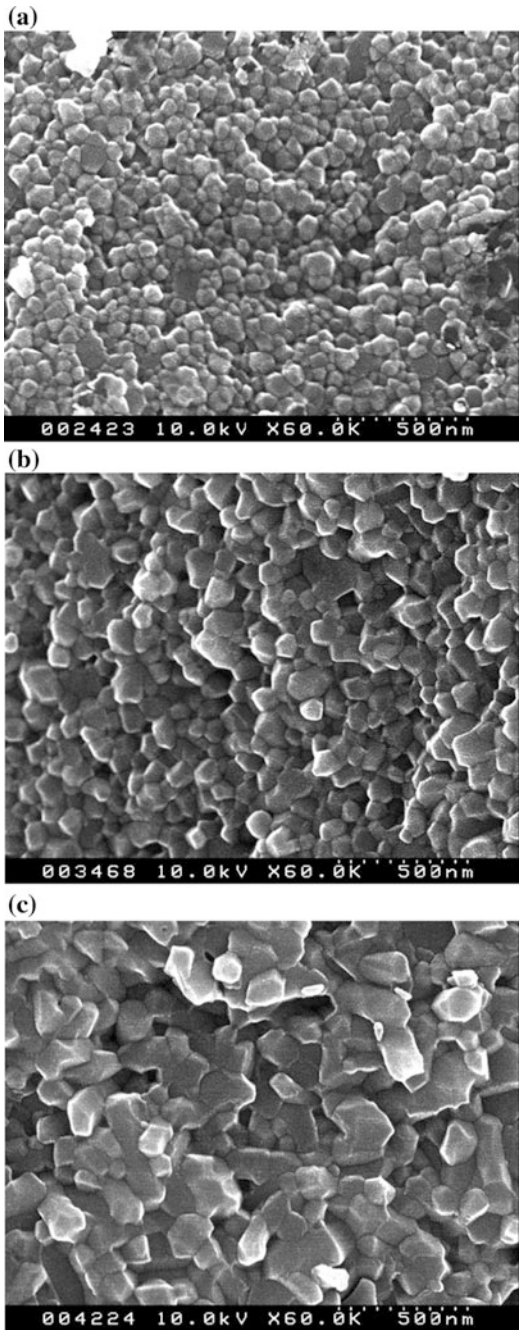

Fig. 2.9 Fracture surfaces of BP2 powder after sintering at different temperatures for 5 min: **a** 1550 °C, **b** 1600 °C, **c** 1650 °C

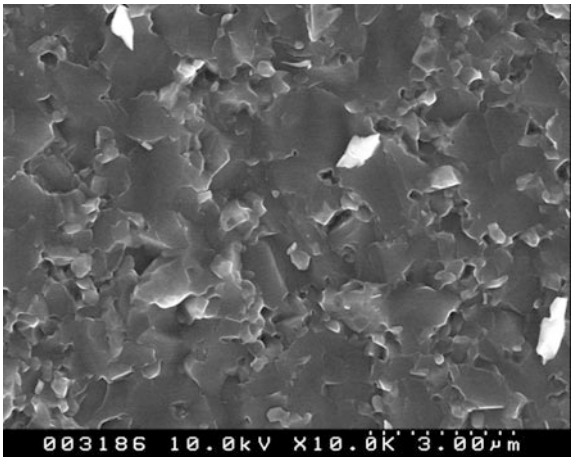

Fig. 2.10 Fracture surface of BP0 powder after sintering at 1700 °C for 5 min

The formation of the liquid phase in the BP0 powder is based on the reactions among Al_2O_3, SiO_2, and the small amounts of AlN and Si_3N_4, where SiO_2 is unavoidably present at the surface of each Si_3N_4 particle. Because of the small amount of sintering additives added and the low reaction rate, the amount of the transient liquid phase is small. In the BP2 powders, as a result of the high-energy mechanical milling, the powders are almost completely mixed and form an amorphous Al–Si–O–N phase, which facilitates the formation of the transient liquid phase and further accelerates the densification process.

Because the amorphous phase in BP2 is far from the conditions for thermodynamic equilibrium, the first stage of densification (particle rearrangement) is accompanied by the rapid precipitation of β-sialon grains. The β-sialon grains precipitate from the liquid phase during the densification of BP2 with a very high driving force, which leads to isotropic grain growth [20]. The large number of uniformly dispersed β-Si_3N_4 nanoparticles in the liquid phase can act as seeds, favor uniform precipitation, and limit the growth of each grain, leading to equiaxed nanosize β-sialon grains.

The amount of particle rearrangement depends on the particle size and shape as well as the amount and viscosity of the liquid phase. The precipitation of β-sialon from BP2 during SPS is delayed at a higher temperature owing to the high heating rate, for which smaller grains and a larger amount of the liquid phase are available to promote rapid rearrangement. This result is in good agreement with that for the sintering of α-sialon [21], for which nearly full densification is achieved through rearrangement within 2 min.

The large particle size and the small amount of the liquid phase in BP0 make it impossible for it to be fully densified at the same temperature as BP2. Furthermore, a shape-accommodating solution-diffusion-reprecipitation process is necessary for the complete densification of BP0, while it is not necessary for the milled powder because grain precipitation accompanies the densification [22].

After the formation of the liquid phase during the sintering of the BP0 powder resulting in better wettability, AlN initially traps the oxide melt to prevent Si_3N_4 dissolution. The preferential dissolution of AlN increases the concentration of Al in the melt, triggering the transient precipitation of supersaturated β-sialon [18]. With the dissolution of Si_3N_4 grains and the precipitation of β-sialon, the Al concentration is decreased. Thus, the initially formed β-sialon grains are richer in Al and O than the overall composition. The solution-diffusion-reprecipitation process is time-consuming, so a longer time is required for complete transformation. In contrast, the formation of β-sialon grains from BP2 is based on the rapid precipitation of a homogeneous nonequilibrium amorphous phase, so the obtained β-sialon grains always have the designed composition ($z \sim 1$) and the phase transformation is rapid.

The full densification of BP2 was achieved in the rearrangement process, so the coarsening (solution-diffusion-reprecipitation) stage was mostly avoided. For the as-received BP0, the formation of β-sialon grains is based on the solution-diffusion-reprecipitation process; most β-sialon grains grow from large β-Si_3N_4 grains [23], resulting in a coarse microstructure. Note that the ceramic obtained from BP0 (1700 °C, 5 min) is composed of only about 40 wt% β-sialon; the small grains in Fig. 2.10 appear to be unreacted β-Si_3N_4, so the grains would be larger if 100 wt% β-sialon was formed.

α-Sialon ($Re_xSi_{12-(m+n)}Al_{(m+n)}O_nN_{16-n}$) ceramics are very attractive for industrial applications where high hardness, wear durability, and oxidation resistance are needed, especially at high temperatures [17]. The proposed method can also be used to prepare nano-sized α-sialon ceramics. Figure 2.11 shows the fracture surface of a dense nano-sized α-sialon ceramic (m = 1.35, n = 0.675).

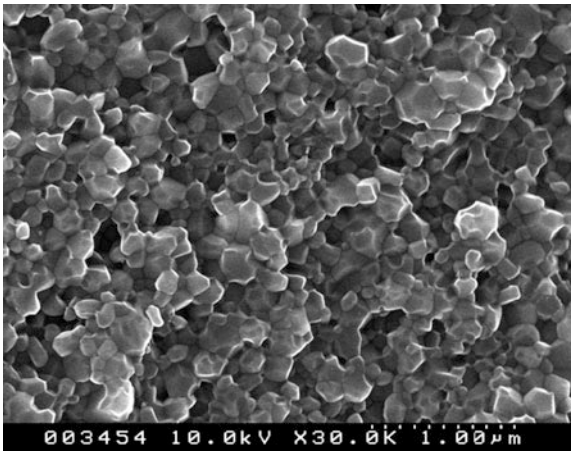

Fig. 2.11 Fracture surface of nano-sized α-sialon ceramic fabricated by spark plasma sintering at 1550 °C for 5 min in nitrogen atmosphere

2.3 Preparation of Dense Nanoscale Si_3N_4/Nanoscale C Metastable Composites

Si_3N_4 ceramics have many tribological applications, which are sometimes in a state of nonlubricated sliding contact. However, the sliding contact of Si_3N_4–Si_3N_4 self-mated tribopairs under dry conditions often has a high friction coefficient and high wear rate [24]. Many researchers have reported self-lubricating Si_3N_4 composites that include carbon, boron nitride, and molybdenum [25, 26]. Among these materials, carbon possesses one of the strongest solid lubricating functions. Hyuga et al. reported that the friction coefficient of a Si_3N_4/carbon fiber composite was around 30 % of that of a monolithic Si_3N_4 ceramic [26]. However, the fracture strength decreased significantly from 950 to 550 MPa when only 1 wt% carbon fiber was added [27], because large carbon fibers acted as sites where fracture originated. Thus, it is very important to decrease the grain size of the added carbon.

On the other hand, nanocomposite materials containing two distinct phases of a material, in which one or both phases are present with nanometer dimensions, have recently attracted considerable interest, because the properties of these materials often differ from those of composites in which the components have large dimensions. Since Niihara proposed the concept of nanocomposite ceramics [28], many researchers have shown that nanocomposites can exhibit improved mechanical properties. Soft and weak materials have also been used as dispersoids. It was reported that the mechanical properties of Si_3N_4 ceramics are improved by nanosize soft and weak ceramic dispersoids such as *h*-BN. For example, 5 vol% BN/Si_3N_4 nanocomposites exhibited improved strength despite a decrease in Young's modulus upon the addition of soft *h*-BN [29]. Thus, the incorporation of nanosize carbon particles is also expected to improve some mechanical properties, such as the fracture strength, and contact-damage resistance.

Since a fine carbon powder will easily react with Si_3N_4, SiO_2, and oxide additives at high temperatures, the addition of carbon to Si_3N_4 powder is a commonly used method to incorporate SiC grains into Si_3N_4 ceramics [30, 31]. It is impossible to prepare Si_3N_4/C nanocomposites through conventional methods. Measures must be taken to prevent reactions occurring between C and the other starting powders.

The starting powders were 90.73 wt% submicrometer β-Si_3N_4 powder with an average particle size of 0.5 μm, 7.85 wt% Y_2O_3, and 1.42 wt% Al_2O_3. The amount of carbon with an average particle size of 5 μm was 5 wt% relative to the weight of the other starting powders. The starting powders were mixed in ethanol using Si_3N_4 balls for 4 h. The as-received powder mixture (denoted as CP0), with a mass of about 6.2 g, was then subjected to high-energy mechanical milling with the same milling parameters as before, except for a longer milling time of 6 h. The amorphization of the starting powders during mechanical milling also occurred and milled powders with a similar internal structure (denoted as CP2) were obtained.

Typical thermal analysis curves for the CP0 and CP2 powders subjected to heating in flowing air are shown in Fig. 2.12. A large weight loss (>4 wt%) was observed for the CP0 powders, which was attributed to the oxidation of carbon.

In contrast, for the CP2 powders, hardly any weight loss was detected, indicating that most of the carbon particles were embedded in the amorphous phase during the milling process. The amorphous phase separates the free carbon from the oxygen in air and prevents their reaction.

The shrinkage curves of the as-received and milled powders are plotted in Fig. 2.13. After sintering at 1600 °C for 5 min, the as-received powders reached only 85 % ρ_{th}, whereas the milled powders were completely densified with a very high densification rate. As shown above, the milled powders contain a large amount of the liquid phase and much finer β-Si_3N_4 particles. This promotes particle rearrangement at a lower temperature with a higher shrinkage rate, enabling full densification to be achieved in a short time. The as-received powders were fully densified at a higher temperature of 1780 °C with the same holding time of 5 min.

The XRD pattern of the CP2 powders after sintering at 1600 °C for 5 min is shown in Fig. 2.14a. The only crystalline phase appearing in the composite was β-Si_3N_4; SiC and other reaction phases could not be detected. For the ceramic obtained from CP0 powders by sintering at 1780 °C for 5 min (Fig. 2.14b, c), the phase composition was not uniform throughout the specimen. SiC was formed near the surface of the specimen, while only β-Si_3N_4 could be detected in the center region.

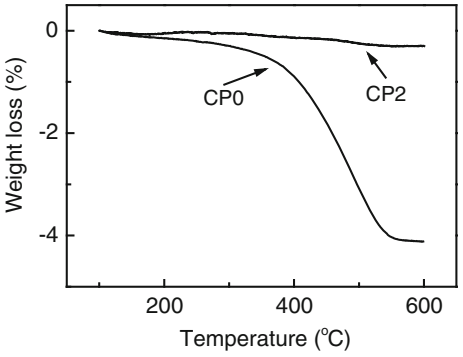

Fig. 2.12 Thermal analysis curves of CP0 and CP2 powders heated in flowing air

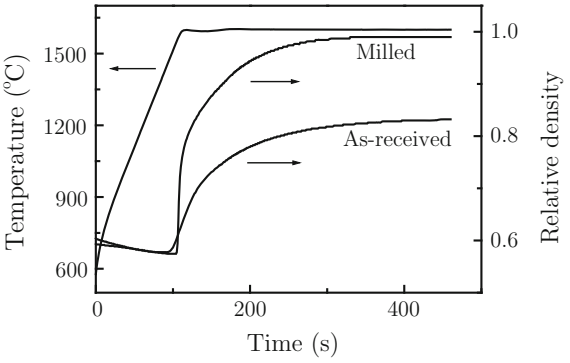

Fig. 2.13 Shrinkage curves of milled and as-received powders

Figure 2.15 shows the Raman spectra of a monoclinic Si_3N_4 nano-sized ceramic (Fig. 2.6) and the composite obtained here. The peaks at 1584 and 1350 cm^{-1} for the composite are the well-known graphite G band and disorder-induced D band, respectively [32], confirming the existence of free carbon in the form of partially amorphous graphite.

The sintered body obtained from the CP2 powders was crushed for TG analysis using the same method as that for the starting powders; a weight loss of about 2.8 % was detected, which was attributed to the oxidation of free carbon. Because the ceramic could not be completely crushed and some carbon grains may have been dispersed within the Si_3N_4 grains, the weight loss was lower than the added carbon content.

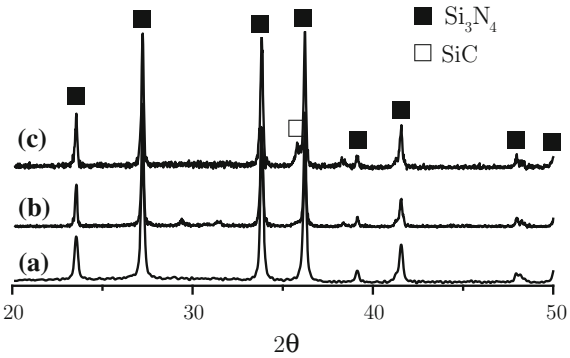

Fig. 2.14 XRD patterns of ceramics obtained by **a** sintering CP2 powder at 1600 °C for 5 min, **b** sintering CP0 powder at 1780 °C for 5 min (inner region), **c** sintering CP0 powder at 1780 °C for 5 min (outer region)

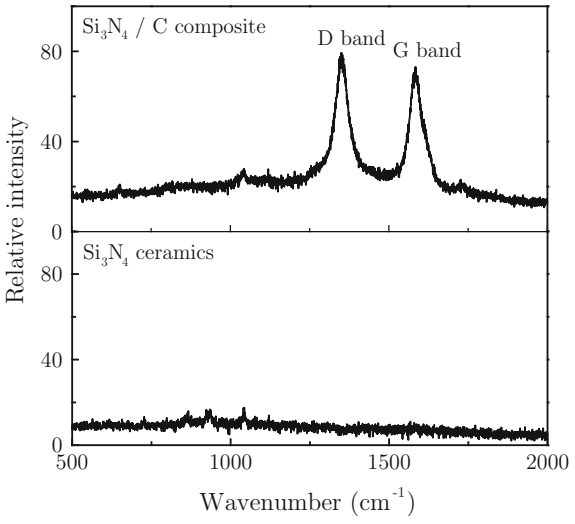

Fig. 2.15 Raman spectra of monoclinic silicon nitride ceramic and the obtained composite

Figure 2.16 shows the sintered microstructures obtained from the CP0 powders (1780 °C, 5 min) and CP2 powders (1600 °C, 5 min). The CP0 powders produce a nanoscale SiC/microscale Si_3N_4 composite. The Si_3N_4 grains in the matrix are homogeneous and most of them are nearly the same size as the grains in the starting Si_3N_4 powder, indicating that SPS is suitable for suppressing grain growth. Newly formed SiC grains with an average diameter of 90 nm agglomerate and disperse within the Si_3N_4 grain boundaries. A nano/nano composite microstructure was obtained from the CP2 powders. From the microstructure of nanosize Si_3N_4 ceramics obtained by the same method (Fig. 2.6), it was concluded that the small grains were carbon, which were homogeneously dispersed in nano-sized Si_3N_4 grain boundaries. The homogeneous dispersion of carbon in the matrix is important for maintaining the mechanical properties, because the aggregration of soft carbon particles causes the deterioration of the mechanical properties. Both Si_3N_4 and C have narrow grain size distributions. The average diameters of carbon grains and silicon nitride grains are 10 and 70 nm, respectively. Although a longer milling time was used, the diameter of Si_3N_4 grains in the obtained nano/nano composite was similar to that in the monolithic Si_3N_4 nanoceramics, because the carbon decreased the milling efficiency by acting as a lubricant.

Figure 2.17 shows TEM images of the obtained nano/nano composite. Figure 2.17a shows a typical nano/nano composite structure, in which nano-sized C particles are homogeneously dispersed at grain boundaries. As shown in the high-resolution image in Fig. 2.17b, the fringe spacing of 0.34 nm is typical of graphite, confirming that the nanograins are carbon. The layer-structured nanoscale C grains are composed of disordered layers, which existed in the grain boundaries of the Si_3N_4 grains. The structure of C shows that it is partially amorphous, which is consistent with the G band and D band observed in the Raman spectra.

Thermodynamic analysis of the possible reactions in the Si–Y–Al–O–N–C system has been performed in many studies [33–35]. Many reactions between the added carbon powder and the other starting powders may occur during sintering:

$$C(s) + SiO_2\ (s) \rightarrow SiO(g) + CO\ (g) \tag{2.2}$$

$$2C(s) + Al_2O_3(s) \rightarrow Al_2O(g) + 2CO\ (g) \tag{2.3}$$

$$2C(s) + Y_2O_3(s) \rightarrow Y_2O(g) + 2CO\ (g) \tag{2.4}$$

$$3C(s) + Si_3N_4(s) \rightarrow 3SiC(S) + 2N_2\ (g) \tag{2.5}$$

All the reversible reactions proceed to the right only if the gaseous reaction products (CO, SiO, Al_2O, Y_2O, N_2) can escape simultaneously. It is very difficult for the gaseous reaction products to move freely by solid-state diffusion. Thus, the reactions may be suppressed by a high densification rate. In this research, the sintered density of the CP2 powders increased to more than 90 % ρ_{th} within 1 min, changing the ceramics from having open porosity to having closed porosity. However, this cannot entirely prevent all the reactions from occurring. The CP0

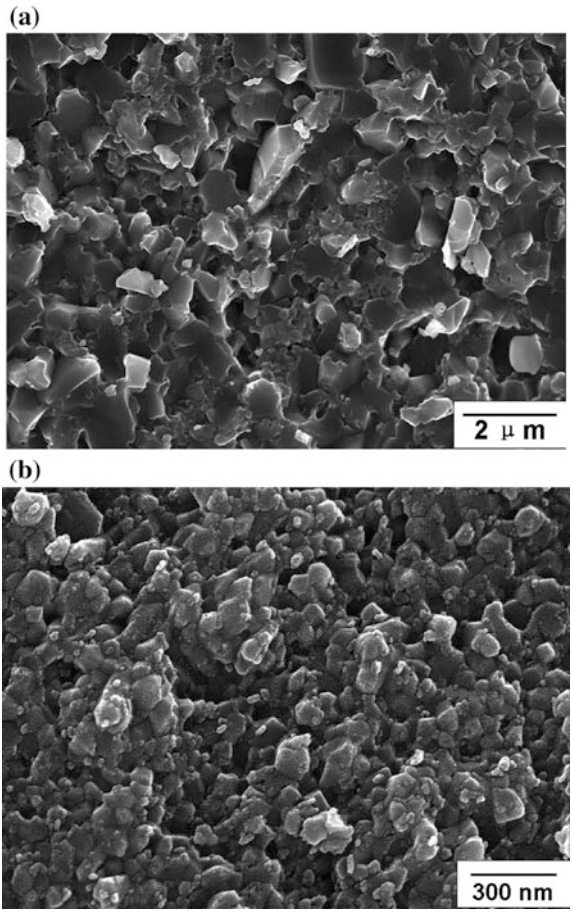

Fig. 2.16 Fracture surfaces of composites obtained by **a** sintering CP0 powders at 1780 °C for 5 min, **b** sintering CP2 powders at 1600 °C for 5 min

powders were also almost completely densified within 1 min at a higher sintering temperature of 1780 °C, whereas the Si_3N_4/C composite was not obtained at this high temperature owing to the high reactivity of carbon particles. SiC is formed through reaction (2.5). There is no carbon or SiC in the inner region and the amount of the newly formed SiC phase is low, indicating that reactions (2.2)–(2.4) might occur during sintering, in which some of the free carbon is transformed into volatile gas and escapes from the specimen. Thus, the achievement of a Si_3N_4/C nano/nano composite may also be related to two other reasons: (1) a lower densification temperature, which leads to smaller driving forces for the reactions proceeding to the right [33]; (2) incorporation of most of the carbon particles into the amorphous phase during milling, which prevents all the possible gaseous reaction products from escaping at the beginning. In conclusion, the high densification rate, the incorporation of carbon particles into the amorphous phase, and the lower sintering temperature prevent all the reactions from occurring, making it possible to prepare a dense Si_3N_4/C nano/nano composite.

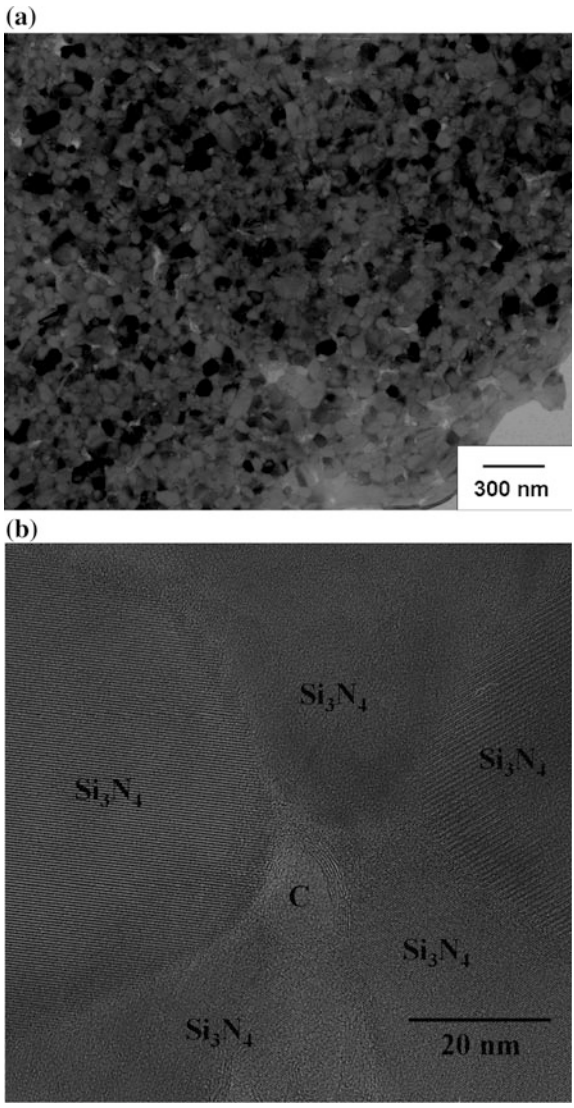

Fig. 2.17 TEM images of the nano/nano composite obtained from CP2 powders: **a** low-magnification image, **b** HRTEM image indicating the Si_3N_4 and C grains

2.4 Superplastic Behavior of Nano-Sized Silicon Nitride Ceramics

As pointed out at the beginning of this chapter, the reason for preparing nano-sized Si_3N_4 ceramics is to achieve superplastic deformation. Thus, the compressive superplastic behavior of nano-sized Si_3N_4 ceramics was next investigated. The microstructure of a Si_3N_4 nanoceramic exhibiting superplastic deformation is

shown in Fig. 2.6. This nanoceramic has nearly equiaxed grains with a diameter of 68 nm.

The deformation of specimens was assessed by uniaxial compression testing, in which compression was applied perpendicular to the direction of SPS. The specimens had a cross-sectional area of 3 mm by 2.5 mm and a height of 5 mm. They were placed between two SiC spacers that were coated with BN to reduce friction. Constant-crosshead-displacement-rate tests were conducted for most of the specimens under a nitrogen atmosphere with a pressure of 0.1 MPa in a furnace with a tungsten heating element. Each specimen was heated up to the test temperature at a rate of 15 °C/min then the test temperature was maintained for 10 min to remove the thermal expansion of the machine system. The displacements of the specimens during deformation were corrected by considering the displacements generated by the elastic deformation of the machine system during loading, which were measured at each temperature in advance. The stress was calculated using the cross-sectional area, assuming that the volume of the specimen was constant during deformation. A limited number of experiments were preformed under constant stress. To ensure constant stress, the load was increased at displacement intervals of 0.05 mm.

2.4.1 Deformation Behavior

Compression tests were carried out at temperatures ranging from 1450 to 1600 °C and at strain rates ranging from 6×10^{-6} to 1×10^{-3} s^{-1}. A typical set of stress versus strain curves obtained during compression are shown in Fig. 2.18. After the initial transient, principally accounted by the elastic response of the specimen, the stress increased linearly with the strain. The increase in stress was attributed mainly to the increase in the strain rate due to the decrease in the specimen height during the deformation tests, as will be discussed later.

To determine the stress exponent, the true stress was plotted against the strain rate on a logarithmic scale for different temperatures. The true stress under the initial strain rate was defined as the intersection of two lines extrapolated to the elastic and plastic strain regions of the stress-strain diagram. Figure 2.19 illustrates the variation in the strain rate with the true stress for specimens tested at different temperatures. The stress exponent n decreases from ~ 2 at low stresses to ~ 1 at high stresses. The trend of n hardly changes with the temperature, except that the transition stress from the region with $n \sim 2$ to the region with $n \sim 1$ is reduced with increasing temperature.

The nano-sized ceramics were also deformed under constant stress. Figure 2.20 shows the deformation curves at 1500 °C under constant stresses of 15 and 50 MPa. The strain-time response of the two specimens includes a small initial elastic deformation upon loading and then an apparent steady-state period up to a strain of 0.45. The strain rates of 9.3×10^{-5} s^{-1} at 50 MPa and 1.8×10^{-5} s^{-1} at 15 MPa are in good agreement with the values obtained by constant-displacement-rate tests, as shown in Fig. 2.19.

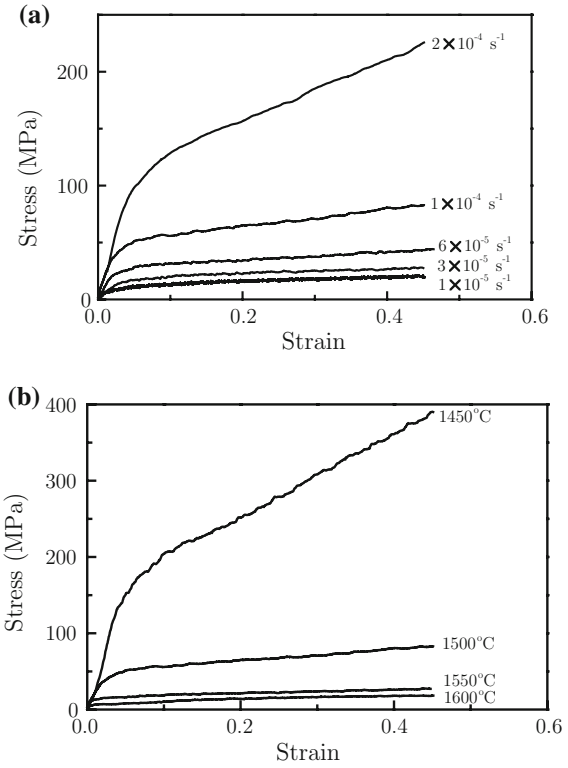

Fig. 2.18 Typical stress-strain curves obtained during compression for nano-sized Si_3N_4 ceramics: **a** at 1500 °C under different initial strain rates, **b** under an initial strain rate of $1 \times 10^{-4}\,s^{-1}$ at different temperatures

The temperature dependence of the superplastic flow was determined by activation energy analysis. The activation energy for superplasticity was obtained from an Arrhenius plot of the strain rate versus the reciprocal of the absolute temperature at a constant flow stress, which is shown in Fig. 2.21. The activation energy is ~852.8 kJ/mol for the $n \sim 2$ region at a stress of 10 MPa and 571.8 kJ/mol for the $n \sim 1$ region at a stress of 100 MPa. The value for the $n \sim 1$ region is in the range of the activation energies previously reported for Si_3N_4 ceramics with Y_2O_3/Al_2O_3 as sintering additives [36, 37], while the value for the $n \sim 2$ region is somewhat higher than those previously reported.

The transitions of both the stress exponent and the activation energy indicate that the deformation mechanism changes with decreasing stress. Thus, the deformation mechanism should be determined separately for the high-stress region and low-stress region from the stress exponent and activation energy, respectively, combined with the microstructural evolution. Actually, given the essential complexity of polycrystalline systems, no single deformation mechanism may completely account for the total deformation; several mechanisms are likely to be simultaneously involved. Only the dominant mechanism will be discussed later.

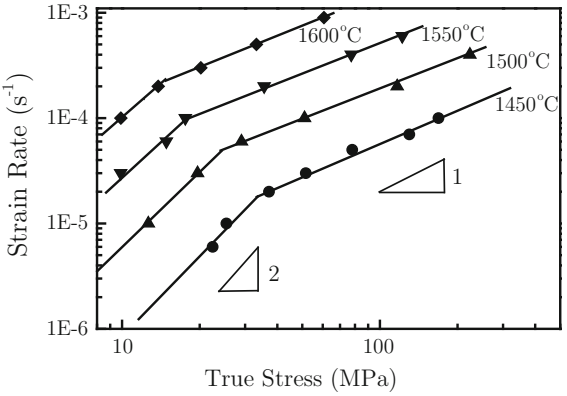

Fig. 2.19 Logarithmic plot of true stress versus strain rate during compression at different temperatures

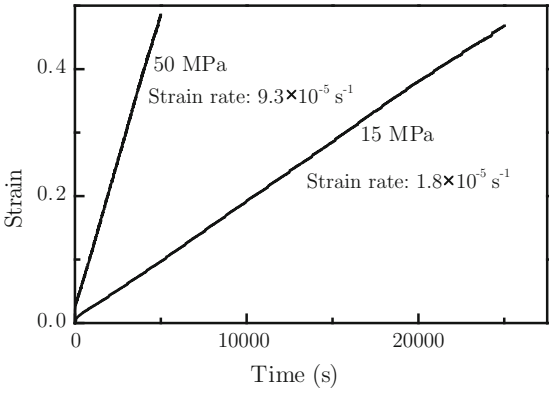

Fig. 2.20 Deformation curves of nanosize ceramics at 1500 °C under constant stresses of 15 and 50 MPa

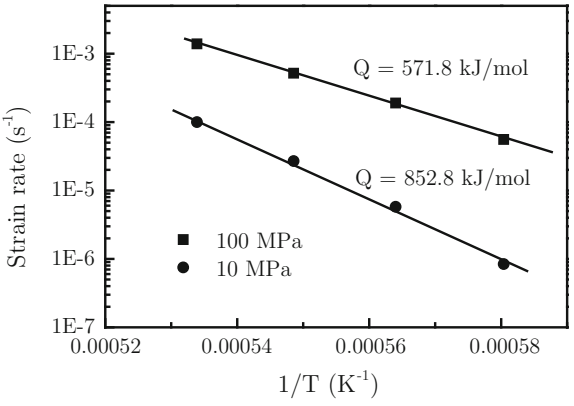

Fig. 2.21 Arrhenius plot of the variation in the strain rate with the inverse temperature for the region with $n \sim 2$ (stress of 10 MPa) and the region with $n \sim 1$ (stress of 100 MPa)

2.4.2 Microstructural Characterization

In all cases, no significant cavitation damage was observed after the compression test, regardless of the temperature, stress, strain rate, and total strain.

Figure 2.22 shows SEM images of specimens deformed at 1500 °C with a strain of 0.45 under initial strain rates of 3×10^{-5} s^{-1} and 10^{-4} s^{-1}. The surfaces are perpendicular to the deformation direction. By comparison with the surfaces of the as-received nanoceramics, it is apparent that concurrent grain growth occurs during the deformation tests. Some equiaxed grains are transformed into rodlike grains during deformation. Under a strain rate of 3×10^{-5} s^{-1}, the grain diameter increases to 145 nm with an average aspect ratio of 3.5, while under strain rate of 10^{-4} s^{-1}, the grain diameter increases to 89 nm with an average aspect ratio of 3.1. The grain growth is more significant at the lower strain rate, indicating that the testing time has a greater influence on dynamic grain growth than stress.

An important characteristic of the deformed material is the development of a preferential orientation of β-Si_3N_4 grains. Phase analysis of the surfaces perpendicular to the deformation direction was carried out using XRD before and after superplastic deformation with a strain of 0.45. The obtained XRD patterns are shown in Fig. 2.23a–c. The XRD pattern of the pulverized state of the as-received ceramic is also shown in Fig. 2.23d. Only β-Si_3N_4 peaks could be detected for all specimens, indicating that the crystallization of grain boundary glassy phase did not occur during the sintering process or deformation tests. Although nearly equiaxed grains were observed in the undeformed ceramic, a slight preferential orientation also developed in the initial undeformed ceramic. The intensity of the (101) and (201) peaks was markedly weakened after deformation, indicating that the elongated β-Si_3N_4 grains are significantly preferentially aligned perpendicular to the direction of superplastic deformation. The extent of texturing is nearly independent of the strain rate.

2.4.3 Deformation Mechanism

2.4.3.1 Deformation at High Stresses

In most cases, accommodated grain boundary sliding makes the dominant contribution to the total compressive deformation of the superplastic flow for fine-grained Si_3N_4 ceramics. This deformation mechanism also appears to operate in nano-sized Si_3N_4 ceramics at high stresses, although the slight grain growth and elongation of β-Si_3N_4 grains occur during the deformation tests.

An accommodation process at triple points is necessary for polycrystalline materials to be deformed continuously without fracture. It is obvious that the accommodation process here is the solution-precipitation process because of the slight grain growth and elongation of β-Si_3N_4 grains. Thus, the rate of grain

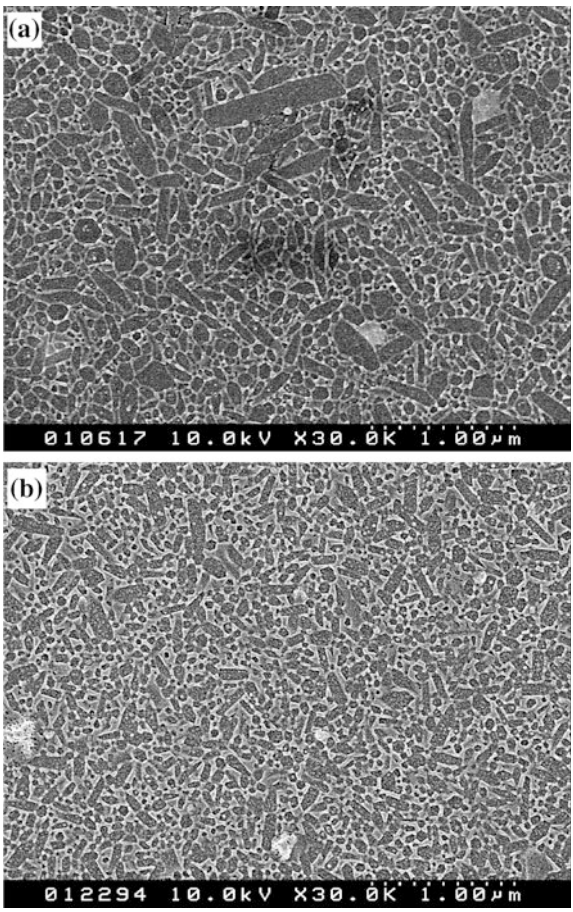

Fig. 2.22 SEM images of specimens after deformation at 1500 °C with a strain of 0.45 under initial strain rates of **a** 3×10^{-5} s^{-1}, **b** 10^{-4} s^{-1}

boundary sliding is controlled by the rate of the solution-precipitation process. The solution-precipitation process in fine-grained ceramics can be controlled by either an interface reaction or by diffusion in the liquid. Lange et al. reported that Si_3N_4 materials with a small amount of the glassy phase had a stress exponent n of unity, corresponding to diffusional creep [38]. From previous studies on the plastic deformation of Y_2O_3/Al_2O_3-doped silicon nitride [36, 37], it also appears that in the domain where accommodated grain boundary sliding is the main factor controlling the strain rate, the solution-precipitation mechanism must be controlled by the diffusion of matter through the glass rather than by the transfer of atoms across the glass/crystal interface [37]. Furthermore, the present experimental activation energy of 571.8 kJ/mol, which corresponds to that for the diffusion of nitrogen ions through the grain boundary glassy phase [36], is similar to other values reported for the deformation of Y_2O_3/Al_2O_3-doped silicon nitride materials for the grain boundary sliding mechanism accommodated by a diffusion-controlled solution-precipitation process [36, 37].

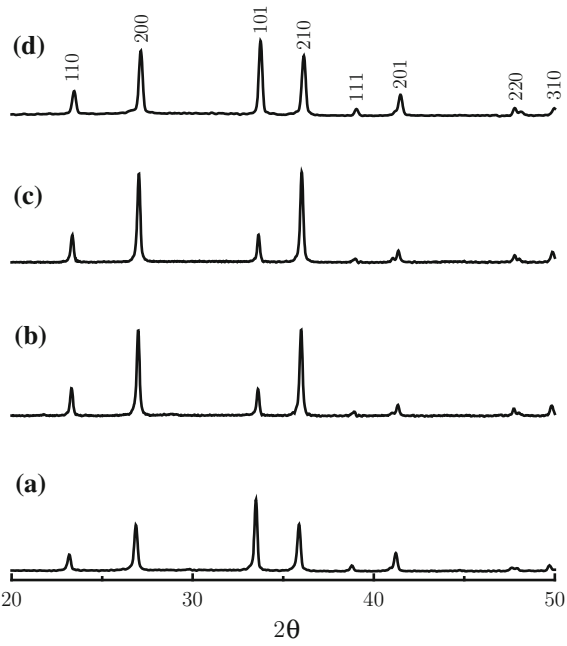

Fig. 2.23 XRD patterns of nanoceramics for surfaces perpendicular to the deformation direction: **a** before deformation, **b** after deformation under a strain rate of 3×10^{-5} s^{-1}, **c** after deformation under a strain rate of 10^{-4} s^{-1}, **d** pulverized state

The stress exponent of unity and the activation energy of 571.8 kJ/mol are thus consistent with the conclusion that grain boundary sliding accommodated by a diffusion-controlled solution-precipitation process is involved in the deformation of nano-sized Si_3N_4 ceramics at high stresses.

2.4.3.2 Deformation at Low Stresses

At low stresses, the data indicate a region with $n \sim 2$ and an activation energy of $\sim$852.8 kJ/mol. Usually, a large value of the stress exponent for Si_3N_4 ceramics is attributed to cavitation [39, 40]. A stress exponent of 2.0 has been reported when studying the creep properties of Si_3N_4-based ceramics [36, 41]. These properties were interpreted using the model proposed by Evans and Rana for materials with a continuous grain boundary phase [42], in which cavities are formed by the viscous flow of the boundary phase in the presence of both an external stress and boundary sliding displacement. Only a low strain can be achieved prior to rupture. In our study, even after a large strain of 1.6 (a reduction in height from 5 to 1 mm), no cracks or large pores could be seen in the polished surface. Thus, the model of cavitation creep is not applicable to the superplasticity of nano-sized Si_3N_4 ceramics.

The significant grain growth that occurred in the nano-sized Si_3N_4 ceramics during deformation tests at lower stresses is clearly the result of the solution-precipitation process. Wakai proposed a “step model” for the solution-precipitation process [43], where different rate-controlling processes yield different stress

exponents. The fundamental hypothesis of his step model is that the solution and precipitation reactions take place at line defects at the grain boundaries, particularly at kinks in the steps formed at grain boundaries. The solution and precipitation of a crystalline material at a step cause its movement, and consequently strain. If the initial density of steps is very low, the two-dimensional nucleation of surface steps occurs, the step density depends on the applied stress, and a stress exponent of $n \geq 2$ can be obtained. On the basis of this mechanism, it is necessary to overcome an energy barrier to form nuclei, the relatively high activation energy should be estimated, which is in good agreement with the higher value that we obtained. The above analysis strongly indicates that the deformation mechanism at low stresses is controlled by the interface-reaction-controlled solution-precipitation process with two-dimensional nucleation.

2.4.3.3 Comparison with Previous Studies

Although many superplastic Si_3N_4-based ceramics have been reported previously, here we show the first direct experimental evidence for a transition involving a decrease in stress from $n \sim 1$ to $n \sim 2$, which can be attributed to nano-sized Si_3N_4 grains.

On the basis of the step model [43], the transition stress σ* between two regions is proportional to $\delta D_L/d$, where δ is the thickness of the liquid film, D_L is the diffusion coefficient in the liquid phase, and d is the grain diameter. σ* decreases with increasing grain size. When the initial grain size is too large, σ* is too small and only diffusion-controlled deformation can be observed experimentally. As summarized in a recent review [3], the compressive creep of Si_3N_4 ceramics with a grain size larger than 200 nm is mostly characterized by a stress exponent of around 1, indicating a diffusion-controlled mechanism. High stress exponents are related to microstructural damage that develops during deformation tests, leading to a very low strain.

2.4.3.4 Characteristics of Flow Curve Under Constant Strain Rate

The instantaneous strain rate depends on the strain in the case of deformation at a constant crosshead speed:

$$\dot{\varepsilon}_\varepsilon = \dot{\varepsilon}_0 \exp(\varepsilon), \tag{2.6}$$

where $\dot{\varepsilon}_\varepsilon$ is the strain rate for compression strain ε and $\dot{\varepsilon}_0$ is the initial strain rate. This equation gives the compensation required for the change in the strain rate generated by the change in height of the specimen during deformation.

Using Eqs. 2.1 and 2.6, the stress under a constant (initial) strain rate $\sigma_{c\varepsilon}$ can be described as

$$\sigma_{c\varepsilon} = \sigma_{\varepsilon} \cdot \left(\frac{\dot{\varepsilon}_0}{\dot{\varepsilon}_{\varepsilon}}\right)^{\frac{1}{n}} = \sigma_{\varepsilon} \cdot \exp(-\frac{\varepsilon}{n}), \tag{2.7}$$

where σ_ε is the observed flow stress at strain ε.

Using $n = 2$ (low-stress region) and $n = 1$ (high-stress region) for the compensation, we can obtain the flow curves under a constant (initial) strain rate. Most of the corrected curves show near steady-state deformation. Figure 2.24 shows typical corrected stress-strain curves for the compression of nano-sized Si_3N_4 ceramics at 1500 °C under strain rates of 3×10^{-5} s^{-1} and 10^{-4} s^{-1}.

As can be seen, a nearly constant flow stress was maintained over a large range of strains after the elastic deformation region, suggesting well-defined steady-state deformation. The steady-state deformation was also confirmed by the deformation test under constant stress, as shown in Fig. 2.20. This differs from other reported superplastic Si_3N_4 ceramics, where pronounced strain hardening was apparently observed when dynamic grain growth occurred during the deformation test. This difference can be attributed to the strongly textured elongated grains developed in our study. In addition to the variation of the chemical potential of Si_3N_4 in the liquid phase induced by the external stress, the different interfacial energy between the crystallographic planes of Si_3N_4 grains increases the driving force for deformation [44] when the texture develops. For elongated grains with an aspect ratio of λ, if the applied stress is normal to the elongated grain axis, the creep rate is accelerated by a factor of $(1 + \lambda)$ [45]. Thus, the increase in shear stress due to grain growth can be compensated by textured elongated β-Si_3N_4 grains. Under a constant strain rate, it is possible to express the stress by the following constitutive relation:

$$\sigma \propto \frac{d^p}{(1+\lambda)}. \tag{2.8}$$

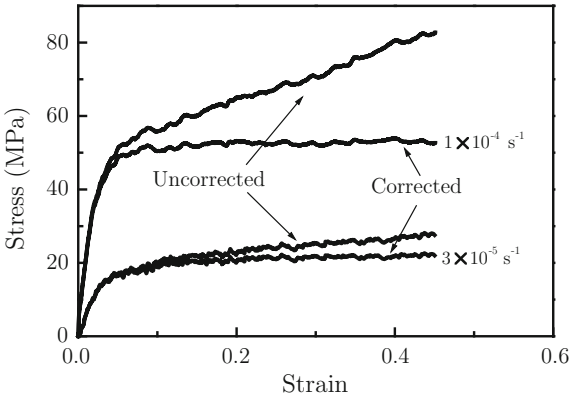

Fig. 2.24 Typical corrected stress-strain curves during the compression of nano-sized Si_3N_4 ceramics at 1500 °C under strain rates of 3×10^{-5} s^{-1} and 10^{-4} s^{-1}

From Eq. 2.8 and Fig. 2.23, it is concluded that $p \sim 1.1$ under a strain rate of 3×10^{-5} s^{-1} and that $p \sim 2.6$ under a strain rate of 10^{-4} s^{-1}. The "p" is a grain-size exponent. Although the grain size exponents for the two regions have not been precisely determined owing to the difficulties in accurately measuring the grain size and texture, the obtained values qualitatively confirm our proposed deformation mechanism.

The classical microstructural requirements for superplasticity in ceramics are fine grains and an equiaxed grain morphology, and most importantly, the microstructure must also be stable because strain hardening often arises from grain growth during a deformation test. From the obtained results, when the grain growth is sufficiently anisotropic to develop texture, it does not influence the steady-state deformation. These well-aligned grains can also produce a fiber-strengthening effect and toughen deformed materials [46].

2.4.3.5 Microstructural Characterization

The elongated Si_3N_4 grains tended to become aligned with their length direction perpendicular to the compressive stress axis, resulting in the development of texture in Si_3N_4 ceramics. The strong texture is assumed to arise from either preferential grain growth or the grain rotation mechanism [47]. In this work, the extent of texturing is nearly independent of the strain rate, although they have different microstructures. It appears that the texture-development mechanisms are different for ceramics deformed under different strain rates (stresses).

At high stresses, grain boundary sliding makes the dominant contribution to the total deformation of the superplastic flow in nano-sized ceramics. When a compressive stress was applied to the as-received ceramics, the grains rotated over each other via grain boundary sliding and the β-Si_3N_4 grains became oriented with their c-axes perpendicular to the stress direction. Simultaneously, oriented β-Si_3N_4 grains in the deformed material grew anisotropically through the diffusion-controlled solution-precipitation process. Thus, the strong texture in the deformed material under high stresses is attributed predominantly to grain rotation via grain boundary sliding and, to a lesser extent, preferential grain growth. At low stresses, the solution-precipitation process makes the dominant contribution to the total deformation. The strong texture is attributed predominantly to the preferential growth of grains aligned perpendicular to the deformation direction and to the solution of grains aligned parallel to the deformation direction.

2.5 Conclusion

(1) High-energy mechanical milling followed by spark plasma sintering was proved to be an effective technique for fabricating nano-sized Si_3N_4-based ceramics and even some metastable Si_3N_4 composites.

(2) Mechanical milling transformed most of the starting powder mixture into an amorphous phase, leading to the homogeneous mixing of the starting powders at the atomic scale. A large amount of nano-crystalline β-Si_3N_4 particles were embedded homogeneously in the non-equilibrium amorphous phase.
(3) The main densification mechanism for the milled powders is particle rearrangement and the phase formation is based on precipitation from the homogeneous amorphous phase on nano-β-Si_3N_4 particles. Rapid sintering of the milled powders at a low temperature can prevent abnormal grain growth, leading to dense nano-sized ceramics.
(4) Investigation of the rate-controlling deformation mechanisms of nano-sized Si_3N_4 ceramics showed that the deformation can be rationalized in terms of two sequential mechanisms. At low stresses, deformation occurred by an interface-controlled solution-precipitation process with two-dimensional nucleation, whereas at high stresses, deformation was controlled by a grain boundary sliding process accommodated by diffusion-controlled solution-precipitation. The strong texture formed during superplastic deformation can compensate the strain-hardening effect arising from concurrent grain growth, leading to near steady-state deformation.

References

1. Riley FL (2000) J Am Ceram Soc 83:245
2. Wakai F, Kodama Y, Sakaguchi S, Murayama N, Izaki K, Niihara K (1990) Nature 344:421
3. Melendez-Martinez JJ, Domingue-Rodriguez A (2004) Prog Mater Sci 49:19
4. Xie RJ, Mitomo M, Zhan GD (2000) Acta Mater 48:2049
5. Rosenflanz A, Chen IW (1997) J Am Ceram Soc 80:1341
6. Hwang SL, Chen IW (1994) J Am Ceram Soc 77:2575
7. Kim BN, Hiraga K, Morita K, Sakka Y (2001) Nature 413:288
8. Mayo MJ, Hague DC, Chen DJ (1993) Mater Sci Eng A 166:145
9. Gleiter H (1989) Prog Mater Sci 33:223
10. Nishimura T, Mitomo M, Hirotsuru H, Kawahara M (1995) J Mater Sci Lett 14:1046
11. Orru R, Licheri R, Locci AM, Cincotti A, Cao GC (2009) Mater Sci Eng R 63:127
12. Li YL, Liang Y, Zheng F, Ma XF, Cui SJ (2000) J Mater Res 15:988
13. Suryanarayana C (2001) Prog Mater Sci 46:1
14. Koch CC (1997) Nanostruct Mater 9:13
15. Kingery WD (1959) J Appl Phys 30:301
16. Hampshire S (2003) J Non-Cryst Solids 316:64
17. Ekstrom T, Nygren M (1992) J Am Ceram Soc 75:259
18. Hwang SL, Chen IW (1994) J Am Ceram Soc 77:165
19. Goto Y, Komatsu M (1999) J Am Ceram Soc 82:1467
20. Herrmann M, Schulz I, Zalite I (2004) J Eur Ceram Soc 24:3327
21. Zenotchkine M, Shuba R, Chen IW (2002) J Am Ceram Soc 85:1882
22. Xu X, Nishimura T, Hirosaki N, Xie RJ, Zhu YC, Yamamoto Y, Tanaka H (2005) J Am Ceram Soc 88:934
23. Akimune Y, Tanimura M, Okamoto Y, Akimune Y, Mitomo M (1994) J Ceram Soc Jpn 102:875

24. Andersson P, Holmberg K (1994) Wear 175:1
25. Iizuka T, Kita H (2005) Wear 258:877
26. Hyuga H, Hirao K, Jones MI, Yamauchi Y (2003) J Am Ceram Soc 86:1081
27. Hyuga H, Jones MI, Hirao K, Yamauchi Y (2004) J Eur Ceram Soc 24:877
28. Niihara K (1991) J Ceram Soc Jpn 99:974
29. Kusunose T, Sekino T, Choa YH, Niihara K (2002) J Am Ceram Soc 85:2678
30. Herrmann M, Schuber C, Rendtel A, Hubner H (1998) J Am Ceram Soc 81:1095
31. Yang JF, Zhang GJ, Kondo N, Ohji T (2002) Acta Mater 50:4831
32. Cancado LG, Pimenta MA, Neves BRA, Dantas MSS, Jorio A (2004) Phys Rev Lett 93:247401
33. Herrmann M, Schuber C, Rendtel A, Hubner H (1998) J Am Ceram Soc 81:1095
34. Watari K, Kawamoto M, Ishizaki K (1989) Mater Sci Eng A 109:89
35. Grande T, Sommerset H, Hagen E, Wiik K, Einarsrud MA (1997) J Am Ceram Soc 80:1047
36. Todd JA, Xu ZY (1989) J Mater Sci 24:4443
37. Crampon J, Duclos R (1997) J Am Ceram Soc 80:85
38. Lange FF, Davis BI, Clarke DR (1980) J Mater Sci 15:601
39. Carroll DF, Tressler RE (1989) J Am Ceram Soc 72:49
40. Wiederhorn SM, Roberts DE, Chuang TJ (1988) J Am Ceram Soc 71:602
41. Arons PM, Tien JK (1980) J Mater Sci 15:2046
42. Evans AG, Rana A (1980) Acta Metall 28:129
43. Wakai F (1994) Acta Metall Mater 42:1163
44. Shinoda Y, Yoshida M, Akatsu T, Wakai F (2004) J Am Ceram Soc 87:1919
45. Emoto H, Mitomo M (1997) J Eur Ceram Soc 17:797
46. Wilkinson DS (1998) J Am Ceram Soc 81:275
47. Lee FJ, Bowman KJ (1992) J Am Ceram Soc 75:1748